Catalysis Science & Technology

ROYAL SOCIETY OF CHEMISTRY

PAPER

View Article Online
View Journal | View Issue

Cite this: *Catal. Sci. Technol.*, 2023, 13, 5214

Two-dimensional (2D) layered double metal cyanides as alternative catalysts for CO_2/propylene oxide copolymerization†

Guillermo Penche, [a] María P. González-Marcos, *[a] Juan R. González-Velasco, [a] Cyler W. Vos [b] and Christopher M. Kozak [b]

Although zinc–cobalt double metal cyanide (DMC) complex is a popular catalyst for the copolymerization of CO_2 and epoxides, it faces important challenges, such as poor CO_2 uptake, high cyclic carbonate formation, low ability to produce high-molecular-weight polymers, and an induction period. Therefore, the pursuit of alternative DMC complexes that can overcome these limitations has been a recurring research strategy in recent years. In this work, four novel 2D layered tetracyanonickelate complexes (M′[Ni(CN)$_4$]; M′ = Ni^{2+}, Co^{2+}, Fe^{2+}, Mn^{2+}) were prepared, thoroughly characterized, and tested as catalysts for CO_2 and propylene oxide copolymerization. These complexes yielded random polyethercarbonates (R_{PEC} = 51–94%) with medium-to-low CO_2 content (F_{CU} = 13.1–42.4 mol%), moderate molecular weight (M_n = 11 000–36 500 g mol^{-1}), and broad dispersity ($Đ$ = 2.5–5.0). The Co–Ni DMC catalyst led to a 100% conversion of PO after 24 h, thus revealing itself as a possible alternative to the classic Zn–Co DMC compound. The catalytic performance of these compounds was compared in detail and their kinetics were assessed by *in situ* IR spectroscopy. While the Co–Ni DMC complex demonstrated remarkable selectivity, it requires further improvements in terms of activity and CO_2 uptake to surpass its counterpart. Future research efforts should focus on driving these critical aspects.

Received 31st May 2023,
Accepted 4th August 2023

DOI: 10.1039/d3cy00753g

rsc.li/catalysis

1 Introduction

Carbon dioxide (CO_2) constitutes the main greenhouse gas (GHG) responsible for global warming of our planet.[1] Its concentration in the atmosphere has increased by up to 50% since the beginning of the industrial revolution and it continues to rise at the highest rate ever observed.[2,3] Urgent action is needed to reverse the situation and prevent the disastrous climatic effects that will surely accompany global warming. Although CO_2-utilization technologies alone cannot solve the problem, they are considered a good complement to carbon capture and storage (CCS) technologies to achieve emission reduction targets.[4] However, the chemical transformation of CO_2 remains problematic due to the high thermodynamic stability and kinetic inertness of this molecule, which is the most oxidized form of carbon. One strategy to overcome these barriers is to use highly reactive electron-rich substrates, such as epoxides, to generate aliphatic polycarbonates (APCs) and/or cyclic carbonates.[5,6] APCs represent an environmentally friendly, biodegradable, and biocompatible alternative to conventional petroleum-based polymers. They find potential applications in a broad range of fields including engineering, biotechnology, medicine, electronics, and so on.[7–14] Although cyclic carbonates are considered highly undesirable by-products when seeking the synthesis of APCs, they also have some interesting industrial applications, such as polar solvents, electrolytes for lithium-based batteries, and reagents.[6,15,16]

Copolymerization of CO_2 and epoxides is among the non-reductive CO_2 conversion methods (*i.e.*, the entire CO_2 moiety is incorporated into the structure without any change in the oxidation state), which means that, using the appropriate catalyst, CO_2 can be activated under mild conditions.[17] Multiple catalytic systems have been screened in the copolymerization of CO_2 and epoxides. There are, in fact, many comprehensive reviews on the different catalysts to which the reader is referred for more detailed information.[18–22] However, the study of catalysts for this technology is still a challenging issue. Prevalent issues are the necessity for substantial catalyst loadings, inferior catalytic activity compared to other commercial polymerizations, and the necessity for expensive, toxic co-catalyst.[23–26]

[a] *Department of Chemical Engineering, Faculty of Science and Technology, University of the Basque Country, UPV/EHU, Campus of Leioa, P.O Box 644, E-48080 Bilbao, Bizkaia, Spain. E-mail: mp.gonzalezmarcos@ehu.eus*
[b] *Department of Chemistry, Memorial University of Newfoundland, St John's, NL, Canada A1B 3X7*

† Electronic supplementary information (ESI) available. See DOI: https://doi.org/10.1039/d3cy00753g

Double metal cyanide (DMC) complexes are a recognized class of catalytic materials for the copolymerization of CO_2 and epoxides. They are conformed of cyanometallate blocks ($[M(CN)_a]^{b-}$) linked together by transition metal cations ($M'^{,c+}$). The resulting metal–cyanide chains (M–C≡N–M′) can be extended by one, two or three dimensions, giving these materials a wide range of different topologies and properties. In general terms, DMCs have the following competitive advantages over other copolymerization catalysts: i) they are inexpensive and easy to prepare, ii) they are insensitive to air and moisture, iii) they do not require co-catalysts, and iv) their heterogeneous nature make them easy to remove from the reaction mixture. As evidenced by the large number of patents[27–35] and academic articles,[36–47] the DMC catalyst based on the combination of the hexacyanocobaltate(III) molecular block ($[Co(CN)_6]^{3-}$) and the Zn^{2+} cation is the most promising DMC compound for large-scale copolymerization of CO_2 and epoxides. Its catalytic activity is so high (*e.g.*, 60 kg polym. g_{cat}^{-1} h^{-1} at 90 °C and a pressure of 40 bar[48]) that subsequent polymer purification is unnecessary. Moreover, its insensitivity to active hydrogen-containing compounds allows the Zn–Co DMC complex to perform controlled polymerizations in the presence of protic chain transfer agents (CTAs).[39–44] This last property makes it especially suitable for the synthesis of low molecular weight CO_2-based polyols destined to be processed as soft segments in the polyurethane (PUR) manufacture industry.[49] However, this catalyst also has some drawbacks. Firstly, it requires large operating pressures to incorporate high amounts of CO_2 into the polymer backbone. Secondly, it yields significant amounts of unwanted cyclic carbonate by-product. Thirdly, although this cannot always be considered as a drawback, the Zn–Co DMC complex gives rise to relatively low-molecular-weight polymers.[19,21] In addition, the Zn–Co DMC complex has an induction time that can extend for hours when working with CTAs.

Consequently, the research trend is moving towards the study of new classes of DMC catalysts. So much so that ten new alternative DMC complexes in CO_2/epoxide copolymerization have been examined over the last two decades,[50–61] including our recent work on evaluation of the catalytic activity of nine unexplored DMCs.[62,63] In this sense, some studies indicate that two-dimensional (2D) layered DMCs could be good candidates to replace the conventional Zn–Co DMC complex.

2D layered DMC materials are composed of single-atom thick sheets built up by the assembly of square planar d^8 cyanometallate anions ($[M(CN)_4]^{2-}$) and divalent transition metal cations (M′,2+).[64] Coates' group[58] evaluated a series of 2D layered materials using cobalt as the external transition metal ($Co[M(CN)_4]$; M = Ni, Pd or Pt) for the copolymerization of CO_2 and propylene oxide (PO) obtaining conversions of PO (X_{PO}) between 13% and 60% after 1 h depending on the metal selected. Among these three 2D materials, the $Co[Ni(CN)_4]$ complex showed the highest activity and selectivity, at 90 °C and 54 bar, to produce high molecular weight polyethercarbonates (PECs) with a moderate content of carbonate units (F_{CU} = 20–36 mol%). Later on, Yu *et al.*[65] verified the great activity of the $Co[Ni(CN)_4]$ complex in epoxide ring-opening polymerizations reporting an impressive productivity of 9.4 kg polym. g_{cat}^{-1} in the PO homopolymerization reaction after 3 h at 90 °C. In 2019, Alferov *et al.*[60] extended the study of the $Co[Ni(CN)_4]$ compound in the CO_2/PO copolymerization reaction by including CTAs. The complex was able to form low-molecular weight PECs (2500–4600 g mol^{-1}) with moderate dispersity (2.5–4.4) using 1,6-hexanediol. However, the catalytic activity was hindered by the presence of such CTAs.

These promising works encouraged us to investigate novel 2D layered DMC materials as potential catalysts for the copolymerization of CO_2 and epoxides. Consequently, in this paper the catalytic performance of the $Ni[Ni(CN)_4]$ (Ni–Ni), $Co[Ni(CN)_4]$ (Co–Ni), $Fe[Ni(CN)_4]$ (Fe–Ni) and $Mn[Ni(CN)_4]$ (Mn–Ni) complexes is studied in the copolymerization of CO_2 and epoxides employing PO as model compound. These materials were synthesized by a *tert*-butyl alcohol (TBA) assisted coprecipitation method, and their physicochemical properties were characterized in depth by different techniques. With this contribution, we intend to open the doors to a new class of DMC catalysts with valuable and advanced structures.

2 Experimental

2.1 Reagents

$NiCl_2$, $CoCl_2$, $FeCl_2$ and $MnCl_2$ salts were purchased from Sigma-Aldrich (Sigma-Aldrich, St. Louis, MO, USA) at 98% purity, and they were used as received. The potassium tetracyanonickelate(II) ($K_2[Ni(CN)_4]\cdot xH_2O$) was acquired from Sigma Aldrich and recrystallized and dried before use. *tert*-Butyl alcohol (TBA) and propylene oxide (PO) were obtained from ACROS Organics (Geel, BE) in 99.5% purity and used without further purification. Toluene in HPLC grade purity (99+%) was used. Air Liquide (Paris, FR) supplied instrument-grade CO_2 (99.99 vol%) in a high-pressure cylinder.

2.2 Preparation of 2D layered DMC compounds

The synthetic procedure used was identical to that reported in previous work[62,63] for other DMC catalysts. Prior to the synthesis, reagents were dried overnight at 100 °C in an oven to remove any trace of water. Details are given below.

Solution 1 was prepared by dissolving 9 mmol of $K_2[Ni(CN)_4]$ in 56 mL of deionized water in a beaker. In another beaker, solution 2 was prepared by dissolving 36 mmol of the $M'Cl_2$ salt in 30 mL of a mixture of TBA and water (TBA/water ratio of 1 : 3 v/v). Solution 1 was heated to 30 °C for 10 min on a hot plate stirrer and solution 2 was added *via* peristaltic pump at a rate of 5 mL min^{-1}. The resulting suspension was aged at the same temperature for 20 min. Subsequently, the formed solid was separated by centrifugation and resuspended in TBA (40 mL) and water

(40 mL) while stirring for 20 min at 30 °C. The solid was again separated by centrifugation and suspended in a mixture of TBA (60 mL) and water (20 mL). This process was repeated once more but suspending the catalysts in 80 mL of pure TBA. Following a final centrifugation, the solid obtained was dried at room temperature in air.

The resulting product corresponds to the hexahydrate form of the cyanonickelate compounds ($M'(H_2O)_2[Ni(CN)_4]\cdot 4H_2O$). To obtain the dehydrated form ($M'[Ni(CN)_4]$), the complexes were dried under vacuum (*ca.* 500 μmHg) at the corresponding dehydration temperature (see section 3.1.2) for 3 h. Once dehydrated, samples remain stable over time without requiring any special storage conditions.

2.3 Instrumentation

Fourier-transform infrared spectroscopy (FTIR) was measured on a Jasco 4200 spectrometer (Jasco Corp., Tokyo, Japan) over the range between 400 and 4000 cm^{-1} at a resolution of 4 cm^{-1}. Samples were analyzed using the KBr-pressed disk technique. The weight ratio of the catalyst to KBr was 1 : 100.

Raman spectroscopy analyses were performed on a Renishaw InVia Raman spectrometer (Renishaw plc, Wotton-under-Edge, UK) using a 514 nm argon ion laser source (Modu-Laser). Samples were analyzed in powder form.

X-Ray diffraction (XRD) analysis was performed on a Bruker D8 Advance diffractometer (Bruker Corp., Billerica, MA, USA) equipped with a HTK2000 high-temperature furnace (Anton Paar GmbH, Graz, Austria). Samples were exposed to Cu Kα radiation (λ = 1.541874 Å) in a continuous scanning mode from an initial value of 2θ = 10° to a final value of 2θ = 70° (step size = 0.033° and step time = 0.8 s). *In situ* high-temperature XRD (HT-XRD) patterns were recorded every 10 °C from 30 to 300 °C in both static air and vacuum. Heating rate was set at 1 °C min^{-1}. ICDD (International Centre for Diffraction Data) cards were used to identify the phases present in the sample by comparison.

Thermogravimetric analysis (TGA) of the catalysts was performed on a TGA SETSYS Evolution instrument (KEP Technologies, Mougins, France) at a heating rate of 1 °C min^{-1} from 25 to 950 °C in both N_2 and air atmosphere. Analysis of the evolved gases was performed with the aid of an HPR-20 EGA quadrupole mass spectrometer (Hidden Analytical, Warrington, UK).

Morphology of the DMC compounds was elucidated by scanning electron microscopy (SEM) and transmission electron microscopy (TEM). SEM images were taken on a Hitachi S4800 SEM (Hitachi Ltd., Tokyo, Japan) operating with a voltage of 10 kV. For the analysis, samples were mounted on aluminum disks using double-sided carbon tape and sputter coated with an ultrathin layer of gold. TEM micrographs were recorded on a JEOL JEM-1400 Plus instrument (JEOL Ltd., Tokyo, Japan) operating at 100 kV with tungsten filament. Samples were dispersed in distilled water with the help of ultrasounds and then the solutions were dropped onto carbon films supported on copper grids.

CHN analysis of the samples was performed on a EuroEA3000 elemental analyzer (Eurovector S.p.A., Pavia, Italy). The equipment was calibrated with acetanilide standard. Samples were burned at 980 °C in a stream of He enriched with O_2. The resulting N_2, CO_2 and H_2O gases were separated in a chromatographic column and measured in a conductivity detector. Callidus® software was used to analyze the peaks.

Wavelength dispersive X-ray fluorescence (WDXRF) analysis of the samples was carried out in the powder form in a PANalytical AXIOS sequential WDXRF spectrometer (Malvern Panalytical Ltd., Malvern, UK) equipped with a Rh tube and three detectors (gas flow, scintillation and Xe sealed).

Textural properties of the solid DMC catalysts were determined by low-temperature (−196 °C) N_2 physisorption using a TRISTAR II equipment (Micromeritics Instrument Corp., Norcross, GA, USA). Prior to analysis, samples were pretreated at 150 °C during 10 h with N_2 flow on a Micromeritics SmartPrep instrument.

The acidity of the samples was evaluated by temperature programmed desorption of NH_3 (NH_3-TPD) on a Micromeritics AutoChem II instrument. Fresh samples were placed on a quartz tube and pretreated at 150 °C under He (50 mL min^{-1}) stream during 3 h for their complete dehydration. Afterwards, samples were cooled down to 100 °C, still in He, and subjected to pulse injections of 6.7 μmol of NH_3 for 10 times. The concentration of NH_3 in the He stream was 2% vol. Subsequently, samples were heated from 100 to 350 °C at 10 °C min^{-1}. Evolved gases were analyzed with an HPR-20 EGA quadrupole mass spectrometer (Hidden Analytical, Warrington, UK). As no water was expected in the samples after complete dehydration, NH_3 consumption was assessed by the signal m/z = 16. For the quantitative analysis, the mass spectrometer signal was converted to NH_3 gas concentration using a concentration calibration.

2.4 Copolymerization of CO_2 and PO

The catalytic activities of the DMC catalysts used here were tested in a 300 mL stainless steel autoclave reactor (Parker Autoclave Engineers, Erie, PA, USA). In a typical copolymerization procedure, a defined amount of catalyst was loaded into the reactor, which was then sealed, purged with N_2 at room temperature for 30 min and evacuated for 1 h at the catalyst dehydration temperature. Both the PO, in the case of bulk polymerization, and the mixture of PO and toluene, in the case of solution copolymerization, were fed using a syringe. After the addition, the reactor was pressurized to 8 bar CO_2 to keep the PO in the liquid phase and speed up the subsequent heating process. Once heated to the desired reaction temperature, more CO_2 was added to achieve a reaction pressure of 20 bar. Pressure was kept constant throughout the reaction by feeding in fresh CO_2 as

it was consumed. After 24 h, the copolymerization was stopped by cooling the reactor in an ice bath followed by depressurizing the vessel. An aliquot was taken immediately after opening the reactor for the determination of conversion. The rest of the product was dissolved in acetone, filtered to remove the catalyst, dried at 40 °C under vacuum for 24 h to remove all volatiles, and analyzed.

In situ monitoring of the copolymerization was carried out in a modified 100 mL stainless-steel reactor vessel (Parr Instruments, Moline, IL, USA) equipped with motorized mechanical stirrer and clamp band heater. For the IR measurements, a ReactIR 45 spectrometer (Mettler Toledo, Greifensee, Switzerland) was used. The spectrometer was equipped with an MCT detector and a SiComp probe which is connected to the base unit *via* a silver-halide DST fiber conduit. The procedure employed for the copolymerization in the 100 mL reactor was identical to that used in the 300 mL reactor with the only difference that the reactor was cooled in a jet of compressed air, rather than in an ice bath, after the reaction.

2.5 Analysis of copolymerization products

Proton nuclear magnetic resonance (^{1}H-NMR) spectroscopic analysis was performed on a Bruker AV500 spectrometer equipped with a 5 mm BBI probed and *Z*-axis gradients, operating at a frequency of 500 MHz. Chemical shifts were referenced with respect to the residual signal of the solvent ($CDCl_3$). The molar content of carbonate units (F_{CU}) in the copolymer backbone, the propylene carbonate (PC) weight percent (W_{PC}) in the product mixture, the CO_2 (S_{CO_2}) and PO (S_{PO}) selectivity towards the polymer, and the polyethercarbonate-to-polycarbonate linkage ratio (R_{PEC}) were determined from the ^{1}H-NMR spectra of the purified products (for more details, see Fig. S1 in the ESI† material). PO conversion (X_{PO}) was calculated from aliquots taken from the reactor immediately after finishing the experiments. In bulk copolymerization, the conversion was determined directly by gravimetry from the difference in weight measured in the sample after a vacuum drying step, at 40 °C until constant weight, in a rotary evaporator. In solution polymerization, X_{PO} was determined from the ^{1}H-NMR spectrum of the fresh product (see Fig. S2†). Normalized integrals were used to determine the concentration of the different contributions.

Size exclusion chromatography (SEC) was used to analyze copolymer weight-average molecular weight (M_w), number-average molecular weight (M_n) and dispersity ($Đ$). Measurements were performed on a Waters Breeze HPLC system (Waters Corp., Milford, MA, USA) equipped with two Styragel columns (HR-4 and HR-1) at 35 °C using tetrahydrofuran (THF) as eluent at a flow rate of 1 mL min^{-1}. The concentration of the samples was 4 mg mL^{-1} and the injection volume 70 μL. Columns were calibrated with monodisperse polystyrene standards.

3 Results and discussion

3.1 2D layered DMCs characterization

3.1.1 Vibrational characterization and crystal structure. The identity of the obtained catalysts was first studied through FT-IR and Raman spectroscopy. DMC complexes are characterized by an absorption band in the range of 2000–2200 cm^{-1} attributed to CN ligand stretching.[66] Fig. 1 displays the ν(CN) region of the samples where three sharp bands corresponding to A_{1g} (Raman active), B_{1g} (Raman active) and E_u (IR active) vibrational modes can be observed. The presence of the IR inactive A_{1g} and B_{1g} modes in the infrared spectrum suggests a slight deviation from the square planar geometry of the $[Ni(CN)_4]^{2-}$ molecular block. The two weak bands at lower frequencies were assigned to the E_u (●) and B_{1g} (■) modes of the $^{13}C^{14}N$ isotope.[67]

In monodentate cyanide compounds, the ligand is bound to the metal *via* the carbon atom (M–C≡N). Bidentate cyanide complexes form inorganic polymeric chains (M–C≡N–M′) by donating the nitrogens lone pair electrons to a second metal. This σ-donation increases the C≡N force constant, resulting in a blue-shift in the frequency of the ν(CN) band frequency.[68] Fig. 1 reveals that the synthesized compounds ν(CN) band frequencies are higher than their linear precursor, which confirms their bimetallic nature. As in the case of other bimetallic cyanide-bridged complexes, the blue-shift is governed by the tendency of the M′ metal to attract electrons toward itself.[62,63] This tendency can be well represented by either the electronegativity or the polarizing power of the M′ metal (Fig. S3†). ESI† provides more details about FT-IR and Raman spectra of the samples (Fig. S4 and Table S1†).

The synthesized 2D layered DMC materials are known to exist in three states of hydration: hexahydrate ($M'(H_2O)_2[Ni(CN)_4]\cdot 4H_2O$), trihydrate ($M'(H_2O)_2[Ni(CN)_4]\cdot H_2O$) and dehydrated/anhydrous ($M'[Ni(CN)_4]$) (Fig. 2). In the hexahydrate form, the M′ metal forms an octahedral coordination with four bridging cyanide ligands and two water molecules on each side of the sheet. Four other water

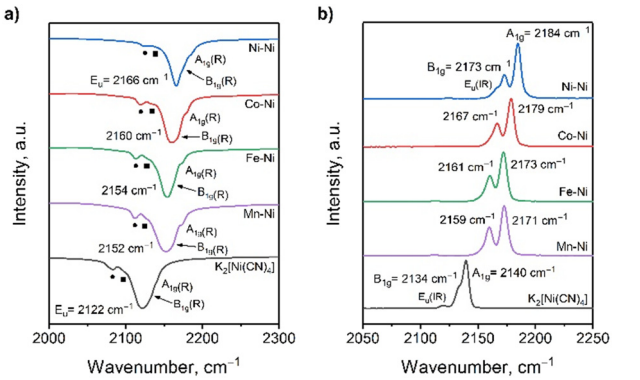

Fig. 1 Vibrational a) infrared and b) Raman spectra of the studied 2D layered DMC materials in the ν(CN) range. ■ B_{1g}, ($^{13}C^{14}N$) and ● E_u, ($^{13}C^{14}N$).

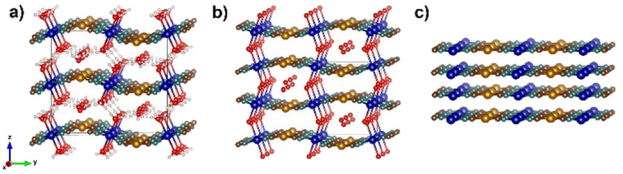

Fig. 2 Crystal structure of the studied 2D layered DMC materials: a) hexahydrate form ($M'(H_2O)_2[Ni(CN)_4]\cdot 4H_2O$), b) trihydrate form ($M'(H_2O)_2[Ni(CN)_4]\cdot H_2O$), and c) dehydrated form ($M'[Ni(CN)_4]$). Color code: M′ centers (blue), Ni centers (golden), N (cyan), C (brown) and O (red). Hydrogen atoms were omitted in the trihydrate form because of the absence of hydrogen bonding.

molecules are held by hydrogen bonds, with one of them weakly interacting with the Ni centers.[69] In the trihydrate structure, the hydrogen-bonded water molecules are lost, causing a misalignment in the sheet curvature relative to each other. While in the hexahydrate state the sheets curvature mimics one another in the trihydrate state the curvature of one sheet is opposite to that of the surrounding sheets. Partial dehydration also causes a decrease in the interlayer spacing of around 1.6 Å. This distance decreases further after complete dehydration of the complexes, when both the M′-coordinated water molecules and the water molecules interacting with nickel are lost. Moreover, upon dehydration, the sheets completely flatten.[64]

Fig. 3 shows the XRD spectra of the samples at each hydration state. The four synthesized complexes are isostructural in both the hexahydrate (ICDD 04-025-6960) and trihydrate (ICDD 04-020-5836) forms. The XRD patterns of the dehydrated forms, however, reveal features characteristic of an amorphous substance, a phenomenon attributed to a disorderly stacking of the sheets.[70] Essentially, the dehydrated structures preserve long-range order in the two dimensions parallel to the layers but lack such long-range periodicity in the stacking direction. This disorder is more prominent in the Ni–Ni and Co–Ni samples.

In hexahydrate materials, the (200) Miller index peak determines the inter-layer spacing. In trihydrate compounds, the *c*-axis indicates the distance between layers, and, therefore, it is now the (002) Miller index peak which determines the distance between two adjacent layers.[64] These peaks are marked in Fig. 3 for each set of XRD patterns. The peak shift from *ca.* 14.5° (*d*-spacing of 6.1 Å) in the hexahydrate form to *ca.* 19.9° (*d*-spacing of 4.5 Å) in the trihydrate form illustrates the sheets approach due to partial dehydration. According to the model proposed by Nash *et al.*,[64] the interlayer distance falls around 3.81 Å in the dehydrated form, so a peak *ca.* 23.3° would correspond to the interlayer spacing. However, this peak could not be identified in Ni–Ni and Co–Ni samples due to the high disorder of their structures.

3.1.2 Dehydration process and thermal stability. Robertson *et al.*[58] reported that only the dehydrated form of the Co–Ni complex exhibited catalytic activity in PO polymerization. We confirmed the negligible activity of all hydrated phases in the copolymerization of CO_2 and PO. This inactivity is associated with the lack of vacant sites for the polymer chain growth, as guest molecules are coordinated. Therefore, it is essential to know the phase-transition temperatures of the complexes. These temperatures were determined by HT-XRD and TGA experiments in different atmospheres. According to the HT-XRD plots (Fig. S5 and S6†), the hexahydrate-to-trihydrate transition occurs between 40–50 °C for all samples in air, while the transition temperature from the trihydrate to the dehydrated form varies depending on the nature of the M′ metal. The Ni–Ni compound exhibits the highest dehydration resistance ($T_{Dehyd.}$ = 140 °C). The Co–Ni, Fe–Ni and Mn–Ni complexes fully dehydrate at 80 °C, with the last two showing an earlier start of the dehydration process (*ca.* 70 °C). Under vacuum (0.015–0.023 mmHg) all samples except the Ni–Ni complex dehydrated at 30 °C. The Ni–Ni compound, therefore, demonstrated to be more reluctant to losing its coordinated water molecules, likely due to the strong Ni–OH_2 interaction caused by Ni^{2+} cations high electronegativity.

Fig. 4 presents the TGA plots of hexahydrate materials in oxidizing and inert atmospheres. Two major stages of weight loss can be distinguished: i) water loss and ii) cyanide

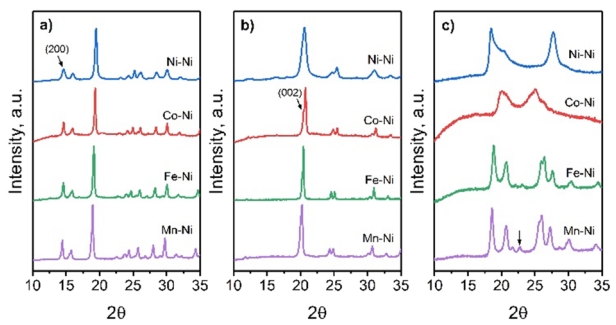

Fig. 3 XRD patterns of the studied 2D layered DMC materials: a) hexahydrate form ($M'(H_2O)_2[Ni(CN)_4]\cdot 4H_2O$), b) trihydrate form ($M'(H_2O)_2[Ni(CN)_4]\cdot H_2O$), and c) dehydrated form ($M'[Ni(CN)_4]$). The arrow indicates the peak corresponding to the space between two contiguous layers.

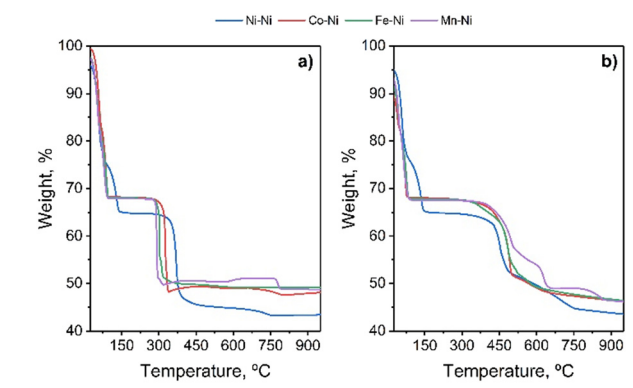

Fig. 4 TGA of the studied 2D layered DMC materials in a) air and b) N_2.

Table 1 Phase transition and decomposition temperatures of the studied 2D layered DMC materials according to the TGA results

	Phase-transition temperature, °C				Decomposition temperature,[a] °C	
	Hexahydrate-to-trihydrate		Trihydrate-to-dehydrated			
Sample	N_2	Air	N_2	Air	N_2	Air
Ni–Ni	90	95	150	150	430	355
Co–Ni	47	70	85	100	415	320
Fe–Ni	50	62	95	100	420	300
Mn–Ni	50	60	100	100	450	290

[a] Temperature at which 5% of the anhydrous sample decomposes.

framework decomposition. All samples display a water content between 32–35% by weight, consistent with the expected 6 water molecules per Ni atom. Water loss occurs between 25–150 °C and comprises two sub-stages (Fig. S7†). The first stage involves the loss of three hydrogen-bonded water molecules, while the second involves the loss of two different water molecules: one corresponding to coordinated water and the other to hydrogen-bonded water weakly interacting with Ni. The transition from the first to the second stage corresponds to the hexahydrate-to-trihydrate transformation. The temperature at which all water molecules are lost corresponds to the dehydration temperature. Decomposition starts above *ca.* 270 °C in air and *ca.* 350 °C in N_2. The decomposition mechanism is different in each atmosphere, as evidenced by the differences in weight loss stages corresponding to the disintegration of the metal–cyanide structure. Table 1 summarizes the phase transition and decomposition temperatures extracted from TGA. DMCs are less stable in oxidizing than in inert atmosphere. However, dehydration begins much later in air due to ambient humidity, which affects both dehydration kinetics and equilibrium moisture content. During dehydration, the loss of two compounds was identified from the analysis of the evolved gases (not shown): water (m/z = 18) and, to a lesser extent, TBA (m/z = 59). Notably, a signal at m/z = 41 was also identified, indicating that part of the TBA is lost in its dehydrated form (isobutylene). The dehydration of TBA at low temperatures in the presence of DMC catalysts has already been reported and it seems to be caused by the catalytic active centers.[63,71] Above the dehydration temperature, no more TBA was observed in the mass spectra, neither in air nor in N_2. This implies that little to no TBA is retained in the samples after dehydration.

3.1.3 Morphology, textural properties, and surface acidity. Morphology of the synthesized materials was analysed by SEM (Fig. 5) and TEM (Fig. 6). It should be noted that due to the vacuum conditions in electron microscopy techniques, the samples were expected to be completely dehydrated for both SEM and TEM analyses. Apart from the Ni–Ni sample, which consists of nanosized pseudocubic particles, the other DMC complexes exhibit a plate-like morphology. Additional TEM images can be found in ESI† material (Fig. S8†). Remarkably, the Mn–Ni sample displayed two well-differentiated particle types that differ in both shape and size (Fig. S9†). No such differentiation was observed in any other sample. This coexistence of two different species in the Mn–Ni sample could be attributed to the use of organic complexing agents (CAs), like TBA, during the synthesis, which has indeed demonstrated to reduce particle size.[62,63] Table 2 provides an overview of the DMC particle morphology, average size, aspect ratio (r_P), surface area (S_P) and surface-to-volume ratio (S_P/V_P). The in-plane size (L) and average thickness (t) both increase with the electronegativity of the M′ metal, following the trend: $Ni^{2+} > Co^{2+} > Fe^{2+} > Mn^{2+}$. However, L increases more than t in percentage terms, resulting in a reduced r_P value or, in other words, a reduction in the anisotropy of the particles. This is especially evident in the Ni–Ni sample, which is composed of nearly cubic particles rather than plate-like particles. The decrease in particle size with increasing electronegativity of the M′ metal also causes an increase in the S_P/V_P ratio. Note that a high surface-to-volume ratio is highly desirable for heterogeneous catalysts.

Textural properties of the studied 2D layered materials were analyzed by N_2 physisorption (see Fig. S10†). The Co–Ni,

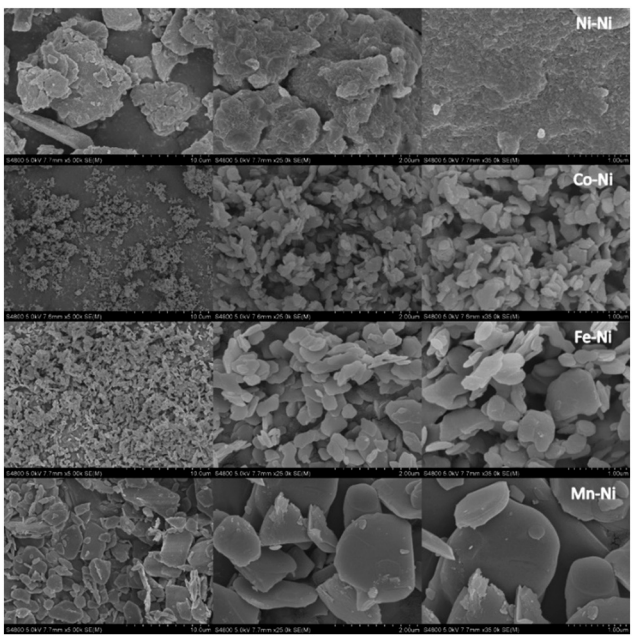

Fig. 5 SEM images of the studied 2D layered DMC materials.

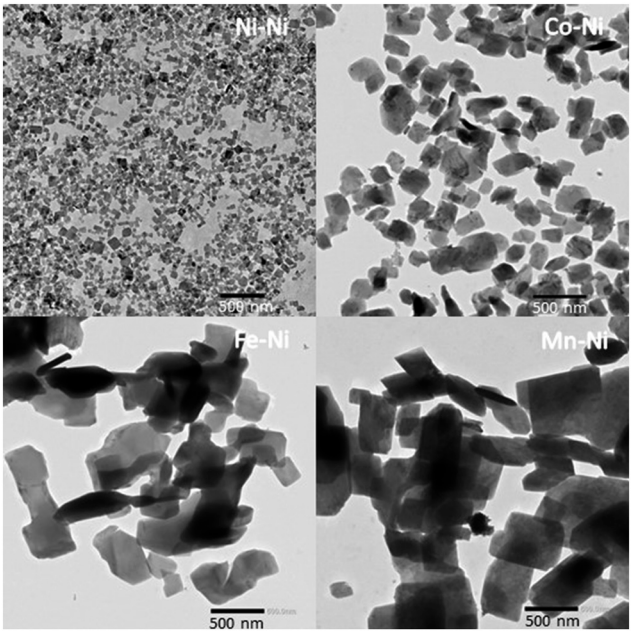

Fig. 6 TEM images (×12k magnification) of the studied 2D layered DMC materials.

Fe–Ni and Mn–Ni samples exhibited type II isotherms with minimal hysteresis loops, indicating the presence of a very small volume of mesopores attributed to interparticle spaces. The Ni–Ni sample showed a type IV isotherm accompanied by a H5 hysteresis cycle. Type H5 loop is unusual, and it is associated with materials containing both open and partially blocked mesopores.[72,73] Particle rearrangement during thermal pretreatment was found to be the cause of this isotherm (Fig. S11, and Table S2†). Dehydration led to Ni–Ni particle agglomeration creating a network of open and partially blocked mesopores. This finding is supported by SEM images, where Co–Ni, Fe–Ni and Mn–Ni samples are seen as a set of discrete laminar particles, while the Ni–Ni sample is seen as a compact agglomerate of well-ordered nanoparticles. Table 3 summarizes the BET specific surface area (S_{BET}), pore size (D_p), and pore volume (V_p). To avoid pore network effects, especially in the H5 hysteresis loop, D_p was derived from the adsorption branch.[73,74] S_{BET}, V_p and D_p values change with particle size. Smaller L resulted in larger S_{BET} and V_p, and smaller D_p. As the electronegativity of M′ determines L, the textural properties of 2D layered DMCs can be adjusted by selecting the suitable M′ metal.

The active sites in the studied 2D layered DMCs consist of coordinately unsaturated M′ centers located on the surface of the complexes. In hydrated forms, the coordination sites are fully filled with N atoms from the CN bridging groups and O atoms from water molecules. Water removal creates open M′ metal sites, which serve as electron-deficient Lewis acid centers. Attempts to find basic or Brønsted acid centers in DMC complexes have consistently failed.[75–77] It is important to note that Ni sites are not considered for catalytic action because their coordination sphere is fully occupied by C atoms from CN linkers. The density and strength of Lewis acid sites in DMC catalysts can be readily determined by selecting a suitable probe molecule and analysis technique. In this study, we evaluated the acidity of the synthesized 2D layered DMC materials using NH_3-TPD (Fig. S12†). Results are shown in Table 3 along with the textural properties. Total surface acidity values are dictated by the S_P/V_P value (or the particle size). In this sense, it is reasonable to think that a higher surface-to-volume ratio should lead to a higher number of exposed M′ metal sites. The number of acid sites per square meter was similar for all samples, except for the Ni–Ni compound, which exhibited slightly higher values due to its particularly small particle size and nearly isotropic shape. Dispersion (D) was calculated by dividing total acidity by the expected number of M′ metal atom per gram (based on the ideal chemical formula: $M'[Ni(CN)_4]$). The values obtained increased with decreasing particle size, but all samples exhibited very low dispersion, which evidences the wide margin for improvement in the optimization of these catalysts.

Regarding the acid sites strength, the Co–Ni sample exhibited the weakest acidity, while the Ni–Ni sample showed

Table 2 Morphological properties of the studied 2D layered DMC materials[a]

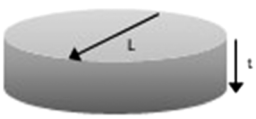

$$r_P = \frac{L}{t}$$

$$S_P = 2\pi\frac{L^2}{4} + 2\pi\frac{L}{2}t$$

$$V_P = \pi\frac{L^2}{4}t$$

Sample	Morphology	L,[b] nm	t,[c] nm	r_P	$S_P \times 10^3$, nm^2	S_P/V_P, nm^2 nm^{-3}
Ni–Ni	Pseudo cubic nanoparticles	46	—	≈1	13	0.166
Co–Ni	Small rectangular and irregular plates	295	65	4.5	221	0.050
Fe–Ni	Medium rectangular and irregular plates	525	79	6.6	616	0.036
Mn–Ni	Medium rectangular and irregular plates	535	157	3.4	820	0.023
	Regular big hexagonal plates	3140	408	7.7	21 140	0.007

[a] Modelled as disks with diameter L and thickness t. [b] Characteristic length determined from TEM images (see Fig. S13†). [c] Average thickness determined from TEM images (see Fig. S14†).

Table 3 Textural and acid properties of the studied 2D layered DMC materials

Catalyst	S_{BET}, $m^2\ g^{-1}$	V_p,[a] $cm^3\ g^{-1}$	D_p,[b] nm	Acidity,[c] $\mu mol\ g^{-1}$	D, %
Ni–Ni	70.4	0.135	8.7	330	7.3
Co–Ni	39.7	0.092	16.5	154	3.4
Fe–Ni	14.5	0.028	19.7	54	1.2
Mn–Ni	3.4	0.005	43.4	12	0.3

[a] Determined by the Gurvich-rule at a relative pressure (P/P_0) of 0.95. [b] Extracted from the Barrett–Joyner–Halenda (BJH) method applied to the adsorption branch. [c] Acidity was calculated by assuming a 1 : 1 stoichiometry for NH_3 adsorption.

the strongest. The Fe–Ni and Mn–Ni samples had medium strength (see ESI,† Table S3). These results align with TGA experiments, in which the Co–Ni sample displayed the weakest M′–OH_2 bond strength and the Ni–Ni sample the strongest, with Fe–Ni and Mn–Ni samples presenting intermediate strength M′–OH_2 bonds. Consequently, the dehydration temperature seems to be a good parameter to estimate the strength of the acid centers, especially when the former is measured in an inert atmosphere, where moisture does not affect the dehydration process.

A question arising from the N_2 physisorption and NH_3-TPD analyses is whether N_2 and NH_3 penetrate in the interlayer space or not. To shed light on this question, the geometric external surface area and the expected density of M′ metal sites on the surface were determined (Table S5†). More information about the calculations is attached in ESI† material. The measured S_{BET} values fall within the range of the calculated geometric external surface areas, suggesting that the area derived from N_2 physisorption is exclusive to the complexes outer surface. This confirms that N_2 does not enter the interlaminar space, which was indeed expected given that the kinetic diameter of N_2 (3.86 Å) is slightly larger than the interlayer space estimated for dehydrated samples (between 3.2 Å (ref. 78) and 3.81 Å (ref. 64)). Since the measured S_{BET} values refer only to the external surface area of the particles, the similarity between calculated and measured acid site densities indicates that NH_3 does not penetrate the interlayer space either. In other words, TPD analysis with NH_3 only measured the acid centers located on the external surface of the particles.

3.1.4 Chemical composition. Chemical composition of the dehydrated samples was evaluated by integrating elemental analysis and WDXRF techniques (Table S7†). The C/N ratio was slightly higher than one in all cases, suggesting the presence of an ancillary carbon source. This implies that we cannot entirely dismiss the presence of TBA on the surface, even though it wasn't detected by TGA-MS nor FT-IR analyses. The M′/Ni ratio increased with the electronegativity of the M′ metal or, what is the same, with the smaller size of the DMC particles. This pattern mirrors previous findings on acidity, wherein the number of M′ sites increased as the S_P/V_P value increased, which, in turn, increased as the particle size decreased. The Cl amount also experienced a dramatic surge as the surface-to-volume ratio increased, suggesting that Cl primarily resides on the surface, likely attached to M′ metal in C≡N–M′–Cl type terminations. Although the precise role of Cl is still unclear, many authors consider it essential to obtain highly active DMC materials.[36,42,79,80]

3.2 Catalytic activity tests

The catalytic performance of the studied 2D layered DMC materials was tested in the bulk copolymerization of CO_2 and PO (Table 4). To ensure accuracy and a complete dehydration, samples were vacuum-dehydrated both before weighing and again in-reactor prior to PO feeding. The 2D layered DMC

Table 4 Catalytic performance of the studied 2D layered DMC materials in the copolymerization of CO_2 and PO

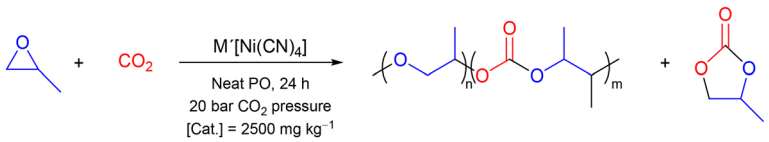

Entry	Catalyst	T, °C	X_{PO},[a] %	F_{CU},[b] mol%	W_{PC},[b] wt%	S_{CO_2},[b] %	S_{PO},[b] %	R_{PEC},[b] %	M_w/M_n,[c] kDa	$Đ$[c]
1	Ni–Ni	90	1	19.7	38.3	33	71	71	—	—
2		120	5	18.4	75.9	8	33	81	—	—
3	Co–Ni	90	100	25.7	0.2	99	100	85	98.7/34.1	2.9
4		120	100	13.9	0.2	99	100	94	89.8/36.5	2.5
5	Fe–Ni	90	19	25.9	4.2	90	97	74	84.9/17.0	5.0
6		120	73	13.1	2.5	89	98	91	60.0/23.8	2.5
7	Mn–Ni	90	8	42.4	5.3	91	96	51	46.6/11.0	4.2
8		120	37	22.0	5.7	85	96	79	46.5/16.9	2.8

[a] Determined by gravimetry. [b] Determined from ^{1}H-NMR (Fig. S18–S25†). [c] Determined by SEC, using THF as eluent, and calibrated using narrow polystyrene standards.

catalysts gave rise to random PECs (R_{PEC} between 51% and 94%) characterized by low-to-medium amounts of carbonate units (F_{CU} between 13.1% and 42.4%) both at 90 °C and 120 °C. CO_2 uptake decreased with temperature, and microstructure randomness increased, which indicates that at higher temperatures, the carbonate units are fewer and more dispersed in the chain. Although PO units should stabilize the copolymer, higher temperatures lead to increased production of PC. This demonstrates the high temperature-dependency of PC formation rates, which is the thermodynamically most favored product. The catalytic activity was quite uneven, with the Co–Ni catalyst emerging as a highly active DMC complex, while the Ni–Ni complex demonstrated minimal activity (X_{PO} = 1% at 90 °C). So was the selectivity (S_{CO_2} between 8% and 99%); while the Co–Ni compound barely produced PC at either 90 °C or 120 °C (W_{PC}, wt% = 0.2), this was the main product in the case of the Ni–Ni catalyst at 120 °C (W_{PC}, wt% = 75.9).

The average molecular weight of isolated copolymers was determined by SEC analysis in THF, calibrated with polystyrene standards (Fig. S15†). For Fe–Ni and Mn–Ni complexes, M_n increased and $Đ$ decreased with temperature due to higher conversion. At low conversion, minor chain length changes led to significant dispersity values. For the Co–Ni sample, which achieved 100% PO conversion at both temperatures, an elevation in temperature resulted in a greater number of chains. Ni–Ni sample produced oligomers near the column detection limit, making the information unreliable. The observed M_n values were lower than expected based on the assumption that each acid site gives rise to one polymer molecule ($M_n = W_{COP}/n_{LAS}$). This discrepancy can be attributed to reversible chain transfer reaction involving adventitious water (or other protic impurities), which leads to an increased number of polymer chains and a consequent decrease in average molecular weight.

The ring-opening copolymerization of CO_2 and PO in the presence of the synthesized 2D layered DMC complexes relies on a crucial initial step involving PO coordination to a Lewis acid center, its activation, and the subsequent attack by nucleophilic species. Since DMCs do not require an exogenous co-catalyst to work, the nucleophilic species must be coordinated to surface Lewis acid centers. Therefore, it can be inferred that catalytic activity represents a balance among the coordination state of active centers, their density, and the concentration of surface nucleophilic species. In this context, the Ni–Ni sample shows the highest density of acid centers, and the highest amount of Cl (the most likely nucleophilic species) in its surface. However, it showed the lowest activity. It thus seems that the coordination state of active sites has the most significant influence on catalytic activity. Electronegativity of M′ metals can serve as a valuable indicator of electron density at Lewis acidic centers. Both selectivity and activity exhibit a volcano-like relationship with the electronegativity of the M′ metal (Fig. S16†), suggesting that very strong Lewis acidity results in a strong alkoxide bond, which hinders the addition of new PO molecules and slows down the nucleophilic attack on coordinated PO. In contrast, very weak acidity leads to a labile alkoxide bond, causing less reactivity of coordinated epoxides. Another useful parameter to measure the metal–oxygen bond strength is the dehydration temperature in an inert atmosphere, which has been found to correlate to some extent with the acid strength observed in NH_3-TPD experiments. The selectivity and activity show a decreasing trend with the increase in dehydration temperature (Fig. S17†). These results would suggest that weak M′–O bond, or Lewis acidity, somehow enhance activity and promote selectivity; however, an optimum was not observed.

3.3 Comparison between the catalytic performance of Co–Ni and Zn–Co DMC complexes

The results in Table 4 highlight the Co–Ni DMC complex as a promising catalyst for CO_2 and PO copolymerization, demonstrating high polymerization yield, moderate CO_2 uptake, selectivity close to 100%, and elevated molecular weight copolymers. As previously noted, the Zn–Co DMC compound currently represents the cornerstone of the DMC catalysts used in epoxide ring-opening reactions, making the industrial feasibility of the Co–Ni DMC complex contingent upon surpassing the formers catalytic performance. Table 5 shows a brief comparison between the catalytic performance of both complexes.

The Zn–Co DMC complex, however, exhibits certain peculiarities that render direct comparison with other DMC catalysts challenging. It is known that, after a short induction period with negligible conversion, the Zn–Co DMC compound undergoes a period of high polymerization rate, which results in severe exothermic reactions that compromise the catalytic performance. For instance, when comparing entry 1 (Table 5) and entry 3 (Table 4), both conducted under identical conditions, the Zn–Co DMC compound demonstrates a diminished performance in relation to the Co–Ni DMC complex, with respect to PO conversion, selectivity, CO_2 uptake and molecular weight. However, these results are influenced by the massive temperature rise observed within the reactor during the copolymerization process (Fig. S26†). By employing a reduced catalyst concentration of 20 mg kg^{-1}, (entry 2, Table 5), overheating was effectively avoided, which yielded a considerable enhancement in CO_2 incorporation and selectivity. The resulting F_{CU} value even exceeded that of the Co–Ni DMC complex; however, PO conversion plateaued at 47% after 24 h of reaction.

Solution polymerization enables better thermal control because the solvents reduce both monomer and catalyst concentrations, lowering the polymerization rate and reducing the heat generated per unit volume. In addition, the viscosity of the reaction mixture also decreases, which helps improve heat transfer.[81] For that reason, entries 3–6 in Table 5 were carried out using toluene as non-reactive solvent. Toluene was selected due to its chemical inertness

Table 5 Comparison of catalytic properties of the Zn–Co DMC and Co–Ni DMC complexes in the copolymerization of CO_2 and PO[a]

Entry	Catal.	Time, h	Copol. tech.	Cat./PO, mg kg^{-1}	X_{PO}, %	F_{CU},[b] mol%	W_{PC},[b] wt%	S_{CO_2},[b] %	R_{PEC},[b] %	M_w/M_n,[c] kDa	$Đ$[c]
1[b]	Zn–Co[d]	1	Bulk[e]	2500	88[g]	8.3	11.1	52	84	16.9/6.9	2.5
2[b]		24		20	47[g]	36.6	2.4	95	70	82.0/40.0	2.1
3[c]		2	Sol.[f]	2500	100[b]	29.6	3.4	92	65	32.3/14.4	2.2
4[c]		8		310	92[b]	39.9	4.5	92	69	61.8/31.2	2.0
5[c]	Co–Ni	2	Sol.[f]	2500	68[b]	22.4	—	100	92	87.0/27.4	3.2
6[c]		24		2500	100[b]	23.8	0.1	100	90	99.1/29.5	3.4

[a] All reaction were carried out at 90 °C and 20 bar. [b] Determined from ^{1}H-NMR. [c] Determined by SEC. [d] Basic characterization in ESI† (Fig. S31). [e] Bulk copolymerization: PO = 41.5 g. [f] Solution copolymerization: PO = 16.6 g, toluene = 26 g. $[PO]_0$ = 5.716 M. [g] Determined by gravimetry.

under the reaction conditions, its high CO_2 dissolution ability and the close similarity between its density and specific heat capacity and those of PO. This choice effectively mitigated temperature increases in the reaction medium. A direct comparison between entry 3 and entry 5 in Table 5 reveals that, when hotspots are avoided, the Zn–Co DMC complex outperforms the Co–Ni DMC in terms of activity and CO_2 incorporation, but with lower selectivity.

The last point is not trivial since the cyclic by-product PC acts as a plasticizer, deteriorating the mechanical and thermal properties of the resulting polymer.[82] Its removal is challenging and implies additional stages in production and higher operational costs. Therefore, keeping PC production as low as possible during copolymerization is highly desirable. Notably, when using Co–Ni DMC compound, the production of PC and the incorporation of CO_2 both decreased compared to the results from bulk polymerization. To determine whether these effects resulted from employing an inert solvent or a shorter reaction time, a new solution copolymerization was conducted with an extended 24 h reaction time (entry 6, Table 5), and the outcomes were compared to those of entry 3 (Table 4). Although W_{PC} value slightly increased with reaction time, it remained negligible and lower than that of bulk copolymerization after 24 hours of reaction. The F_{CU} value also experienced a minor increase, suggesting that CO_2 incorporation is favored during final reactions stages, although it remained still lower than in bulk copolymerization. Consequently, it appears that the presence of toluene lowers both PC production (see Fig. S27†) and CO_2 incorporation, parameters that tend to be correlated.

If the average molecular weight of polymers generated by the Zn–Co and Co–Ni DMC complexes at complete conversion are compared (entry 3 and entry 6, Table 5), it becomes evident that the latter yields significantly longer chain polymers. This outcome aligns with expectations, given that the total acidity of the Co–Ni DMC complex is considerably lower than that of the Zn–Co DMC compound (Fig. S28†). To compare the molecular weight produced by both complexes at equivalent monomer-to-initiator ratio, a fourth reaction was executed (entry 4, Table 5). In this instance, the concentration of the Zn–Co DMC was adjusted so that the number of acid centers exposed in the reaction medium matched that of entry 6 ($[M'] = 3.2 \times 10^{-5}$ mol mL^{-1}). Although the M_n values returned by both catalysts came close, a notable difference emerges in $Đ$ values. The higher dispersity generated by the Co–Ni DMC complex is ascribed to its lower activity, which accentuates the impact of chain transfer reactions with adventitious water.

3.3.1 Co–Ni *vs.* Zn–Co DMC complexes: an *in situ* IR study. The main paragraph text follows directly on here. The catalytic behavior of both complexes in the copolymerization of CO_2 and PO was further evaluated through an *in situ* IR study. The evolution of the reaction was evaluated from a series of key vibrational bands, including i) the ring-deformation mode of PO at 830 cm^{-1}, ii) the ether linkage (C–O–C) in homopolymeric ether units at 1100 cm^{-1}, iii) the carbonyl bond (C═O) in polymeric carbonate units at 1745 cm^{-1} and iv) the carbonyl bond (C═O) in the cyclic carbonate by-product at 1800 cm^{-1} (see Fig. S29 and S30†). PO conversion was monitored from the IR spectra using the Beer–Lambert law (for more information, see ESI†). The conversion and the instantaneous reaction rate curves are attached in Fig. 7.

Results show that the Zn–Co DMC complex reaches complete conversion in 15 minutes, while the Co–Ni DMC complex requires more than 15 hours. However, it is noteworthy that during the first hour of reaction, the Co–Ni

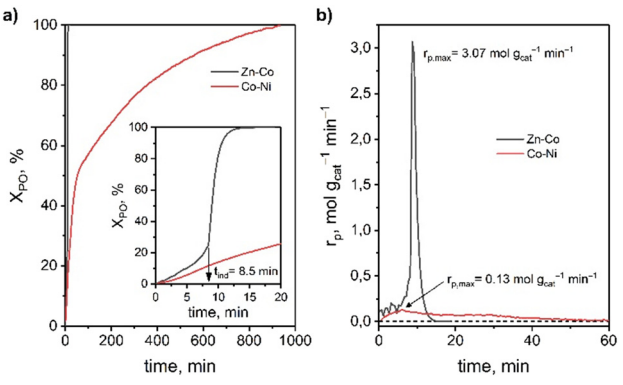

Fig. 7 Curves of a) conversion (inset: close-up on the initial reaction moments) and b) instantaneous reaction rate for the copolymerization of CO_2 and PO in the presence of the Zn–Co DMC (black) and Co–Ni DMC (red) complexes. Reaction conditions: [Cat.] = 975 mg kg^{-1} (Cat./PO = 2500 mg kg^{-1}), [PO] = 5.716 M, P_{CO_2} = 20 bar, T = 90 °C, toluene = 30 mL.

DMC complex consumes most of the PO ($X_{PO} \approx 50\%$), and then a decline in activity is observed likely due to mass transport limitations resulting from increased viscosity of the mixture. The Zn–Co DMC complex exhibits an induction period of approximately 8.5 minutes, which is attributed to the substitution of labile ligands by PO molecules. In contrast, the active centers of the Co–Ni DMC complex are mostly naked in their dehydrated form, and thus no substitution is required. The absence of an induction time represents an important advantage, as it eliminates the need for a pre-activation stage that would require operating in cycles. The Zn–Co DMC complex shows a maximum polymerization rate of 3.07 mol g_{cat}^{-1} min^{-1}, which is much higher than the maximum polymerization rate shown by the Co–Ni complex (0.13 mol g_{cat}^{-1} min^{-1}). Expressed on a per-site basis as turnover frequency (TOF, calculated by dividing the maximum polymerization rate by the total surface acid sites) the performance of both catalysts was closer, although the Zn–Co DMC complex (TOF = 2456 mol PO mol^{-1} M′ min^{-1}) remains more active than the Co–Ni DMC (TOF = 844 mol PO mol^{-1} M′ min^{-1}). This means that the Zn–Co DMC complex not only has a higher concentration of acid centers, but these centers have, on average, a higher catalytic activity, after the induction period.

4 Conclusions

2D layered DMC materials were successfully synthesized through a TBA-assisted coprecipitation method, combining four different divalent transition metal cations (M′ = Ni^{2+}, Co^{2+}, Fe^{2+}, and Mn^{2+}) with the square-planar tetracyanonickelate ($[Ni(CN)_4]^{2-}$) block. Their bimetallic nature was confirmed through IR and Raman spectroscopy. Three distinct hydration states were discerned, with the dehydration temperatures decreasing in the order Ni^{2+} > Mn^{2+} > Fe^{2+} > Co^{2+}. Hydrated forms proved to be catalytically inactive. SEM and TEM verified the plate-like morphology of the solids and evidenced a dependence of the size and thickness of these plates on the M′ metals electronegativity. This morphology in turn governed concentration of the coordinatively unsaturated M' centers (Lewis acid sites), as well as the concentration of other surface species of interest, such as Cl.

All complexes showed to be active in the CO_2/PO copolymerization at both 90 °C and 120 °C under 20 bar CO_2 pressure. The products were PECs with low-to-medium CO_2 content (F_{CU} ranging from 13.1 to 42.4 mol%), medium-to-high molecular weights (M_n = 11 000–36 500 g mol^{-1}), and high dispersity values ($Đ$ = 2.5–5.0). Undesired PC formation varied significantly (W_{PC} between 0.2 and 75.9 wt%). The coordination status of active centers appeared to be the main parameter influencing catalytic performance. Activity and selectivity demonstrated a volcano-like relationship with the electronegativity of the M′ metal, while showing a decreasing relationship with the strength of the M′-O bond, as represented by the dehydration temperature.

The Co–Ni complex emerged as the most promising catalyst, achieving 100% PO conversion after 24 hours with minimal PC production. When compared to the classical Zn–Co DMC complex, the Co–Ni DMC catalyst, while exhibiting lower catalytic activity and reduced CO_2 incorporation, outperforms in several key areas: i) it has superior CO_2 selectivity, ii) produces higher average molecular weight polymers, iii) lacks induction time, and iv) offers easier heat management during copolymerization.

In summary, although the Co–Ni DMC complex is shown as a promising catalyst for the copolymerization of CO_2 and PO at industrial level, further research is required to gain a deeper understanding of the underlying mechanism, enhance CO_2 incorporation, and increase acid center density to narrow the activity gap with the Zn–Co DMC catalyst.

Author contributions

Guillermo Penche: conceptualization, visualization, investigation, methodology, writing – original draft. María P. González-Marcos: conceptualization, visualization, validation, supervision, writing – review & editing. Juan R. González-Velasco: validation, supervision, project administration, funding acquisition, writing – review & editing. Christopher M. Kozak: conceptualization, validation, supervision, funding acquisition, writing – review & editing. Cyler W. Vos: visualization, investigation, methodology, writing – review & editing.

Conflicts of interest

The authors declare they have no known competing financial interests or personal relationships that could have appeared to influence the work reported in this paper.

Acknowledgements

This research was funded by the Spanish Ministry of Science and Innovation (Project PID2019-105960RB-C21 by MCIN/AEI/10.13039/501100011033) and the Basque Government (Project IT1509-2022). GP thanks the Basque Government for his PhD grant (PRE_2021_2_0260) and PhD training fellowship (EP_2022_1_0020). CMK thanks NSERC for a Discovery Grant and the Canada Foundation for Innovation and the Government of Newfoundland and Labrador for infrastructure funding. CWV thanks Memorial University of Newfoundland and Labrador for a Graduate Studies Fellowship. The authors acknowledge the technical and human support provided by SGIker (UPV/EHU Advanced Research Facilities/ERDF, EU).

References

1 US Global Change Research Program, USGCRP Indicator Platform, Annual Greenhouse Gas Index, **https://www.globalchange.gov/browse/indicators/annual-greenhouse-gas-index**, (accessed May 2023).

2 A. Bermejo-López, B. Pereda-Ayo, J. A. Onrubia-Calvo, J. A. González-Marcos and J. R. González-Velasco, *J. CO2 Util.*, 2022, **58**, 101922.
3 A. Bermejo-López, B. Pereda-Ayo, J. A. González-Marcos and J. R. González-Velasco, *J. CO2 Util.*, 2019, **34**, 576–587.
4 I. Ghiat and T. Al-Ansari, *J. CO2 Util.*, 2021, **45**, 101432.
5 Q. Liu, L. Wu, R. Jackstell and M. Beller, *Nat. Commun.*, 2015, **6**, 5933.
6 E. Alper and O. Y. Orhan, *Petroleum*, 2017, **3**, 109–126.
7 T. Artham and M. Doble, *Macromol. Biosci.*, 2008, **8**, 14–24.
8 Y. Xu, L. Lin, M. Xiao, S. Wang, A. T. Smith, L. Sun and Y. Meng, *Prog. Polym. Sci.*, 2018, **80**, 163–182.
9 H. Cao and X. Wang, *SusMat*, 2021, **1**, 88–104.
10 S. Ye, S. Wang, L. Lin, M. Xiao and Y. Meng, *Adv. Ind. Eng. Polym. Res.*, 2019, **2**, 143–160.
11 B. Song, A. Qin and B. Z. Tang, *Cell Rep. Phys. Sci.*, 2022, **3**, 100719.
12 W. Yu, E. Maynard, V. Chiaradia, M. C. Arno and A. P. Dove, *Chem. Rev.*, 2021, **121**, 10865–10907.
13 J. Xu, E. Feng and J. Song, *J. Appl. Polym. Sci.*, 2014, **131**, 39822.
14 R. Muthuraj and T. Mekonnen, *Polymer*, 2018, **145**, 348–373.
15 P. P. Pescarmona, *Curr. Opin. Green Sustainable Chem.*, 2021, **29**, 100457.
16 J. H. Clements, *Ind. Eng. Chem. Res.*, 2003, **42**, 663–674.
17 M. Aresta and A. Dibenedetto, *Dalton Trans.*, 2007, 2975–2992.
18 G. W. Coates and D. R. Moore, *Angew. Chem., Int. Ed.*, 2004, **43**, 6618–6639.
19 Y. Qin and X. Wang, *Biotechnol. J.*, 2010, **5**, 1164–1180.
20 C. M. Kozak, K. Ambrose and T. S. Anderson, *Coord. Chem. Rev.*, 2018, **376**, 565–587.
21 M. R. Kember, A. Buchard and C. K. Williams, *Chem. Commun.*, 2011, **47**, 141–163.
22 F. D. Monica and C. Capacchione, *Asian J. Org. Chem.*, 2022, **11**, e202200300.
23 C. A. L. Lidston, S. M. Severson, B. A. Abel and G. W. Coates, *ACS Catal.*, 2022, **12**, 11037–11070.
24 W. T. Diment, W. Lindeboom, F. Fiorentini, A. C. Deacy and C. K. Williams, *Acc. Chem. Res.*, 2022, **55**, 1997–2010.
25 G. A. Bhat and D. J. Darensbourg, *Green Chem.*, 2022, **24**, 5007–5034.
26 M. A. Rudolph, P. Isbrücker and R. Schomäcker, *Catal. Sci. Technol.*, 2023, **13**, 3469–3482.
27 W. J. Kruper and D. J. Swart, *US Pat.*, US4500704A, Dow Chemical Co., 1985.
28 J. Kuyper, P. W. Lednor and G. A. Pogany, *US Pat.*, US4826953A, Shell USA Inc., 1989.
29 A. Wolf, S. Grasser, C. Gürler and J. Hofman, *US Pat.*, US9080010B2, Covestro Deustchland AG, 2015.
30 J. Hofmann, C. Gürtler, S. Grasse and A. Wolf, *US Pat.*, US9315622B2, Covestro Deustchland AG, 2019.
31 K. W. Haider, K. G. McDaniel, J. E. Hayes and J. Shen, *US Pat.*, US20080021154A1, Covestro LLC, 2008.
32 M. Kember, R. Kabir and C. K. Williams, *US Pat.*, US20180148539A1, Econic Technologies Ltd., 2018.
33 M. D. Blanco González, M. García Ruiz and J. P. González Rivero, *US Pat.*, US10385164B2, Repsol S.A., 2019.
34 K. G. McDaniel, *US Pat.*, US9562135B1, Covestro LLC, 2017.
35 X. Zhang, G. Qi, B. Wei and X. Sun, *US Pat.*, US9469722B2, Zhejiang University ZJU, 2016.
36 J. Sebastian and D. Srinivas, *Appl. Catal., A*, 2014, **482**, 300–308.
37 C. H. Tran, S. A. Kim, Y. Moon, Y. Lee, H. M. Ryu, J. H. Baik, S. C. Hong and I. Kim, *Catal. Today*, 2021, **375**, 335–342.
38 R. Mbabazi, O. F. Wendt, S. A. Nyanzi, B. Naziriwo and E. Tebandeke, *Results Chem.*, 2022, **4**, 100542.
39 Y. Gao, Y. Qin, X. Zhao, F. Wang and X. Wang, *J. Polym. Res.*, 2012, **19**, 9878.
40 S. Chen, Z. Hua, Z. Fang and G. Qi, *Polymer*, 2004, **45**, 6519–6524.
41 S. Liu, Y. Qin, L. Qiao, Y. Miao, X. Wang and F. Wang, *Polym. Chem.*, 2016, **7**, 146–152.
42 S. F. Stahl and G. A. Luinstra, *Catalysts*, 2020, **10**, 1066.
43 Y. Gao, L. Gu, Y. Qin, X. Wang and F. Wang, *J. Polym. Sci., Part A: Polym. Chem.*, 2012, **50**, 5177–5184.
44 N. An, Q. Li, N. Yin, M. Kang and J. Wang, *Appl. Organomet. Chem.*, 2018, **32**, e4509.
45 J. Sebastian and D. Srinivas, *Appl. Catal., A*, 2015, **506**, 163–172.
46 W. Zhang, T. Fan, Z. Yang, R. Yu, X. Zeng, Y. Xu, X. Zeng, Y. Xu, M. Zhang, H. Hu, J. Z. Qu and L. Zheng, *Appl. Mater. Today*, 2022, **26**, 101352.
47 Y. H. Seo, Y. B. Hyun, H. J. Lee, J. W. Baek, H. C. Lee, J. H. Lee, J. Lee and B. Y. Lee, *J. CO2 Util.*, 2021, **53**, 101755.
48 Z. Li, Y. Qin, X. Zhao, F. Wang, S. Zhang and X. Wang, *Eur. Polym. J.*, 2011, **47**, 2152–2157.
49 J. Langanke, A. Wolf, J. Hofmann, K. Böhm, M. A. Subhani, T. E. Müller, W. Leitner and C. Gürtler, *Green Chem.*, 2014, **16**, 1865–1870.
50 X. H. Zhang, S. Chen, X. M. Wu, X. K. Sun, F. Liu and G. R. Qi, *Chin. Chem. Lett.*, 2007, **18**, 887–890.
51 Z. Guo and Q. Lin, *J. Mol. Catal. A: Chem.*, 2014, **390**, 63–68.
52 W. Zhang, Q. Lin, Y. Cheng, L. Lu, B. Lin, L. Pan and N. Xu, *J. Appl. Polym. Sci.*, 2012, **123**, 977–985.
53 C. Dai, Q. Zhu, H. Pang, L. Zhu and Q. Lin, *Mater. Lett.*, 2016, **180**, 89–92.
54 W. Zhang, L. Lu, Y. Cheng, N. Xu, L. Pan, Q. Lin and Y. Wang, *Green Chem.*, 2011, **13**, 2701–2703.
55 L. Qiang, G. Zhifang, P. Lisha and X. Xue, *Catal. Commun.*, 2015, **64**, 114–118.
56 S. Chen, Z. Xiao and M. Ma, *J. Appl. Polym. Sci.*, 2008, **107**, 3871–3877.
57 Z. Guo, Q. Lin, L. Zhu, X. Wang, Y. Niu, C. Yu and T. Fang, *Nanosci. Nanotechnol. Lett.*, 2014, **6**, 353–356.
58 N. J. Robertson, Z. Qin, G. C. Dallinger, E. B. Lobkovsky, S. Lee and G. W. Coates, *Dalton Trans.*, 2006, 5390–5395.
59 M. J. Yi, S. H. Byun, C. S. Ha, D. W. Park and I. Kim, *Solid State Ionics*, 2004, **172**, 139–144.
60 K. Alferov, S. Wang, T. Li, M. Xiao, S. Guan and Y. Meng, *Catalysts*, 2019, **9**, 632.

61 Z. Guo, Q. Lin, X. Wang, C. Yu, J. Zhao, Y. Shao and T. Peng, *Mater. Lett.*, 2014, **124**, 184–187.
62 G. Penche, J. R. González-Velasco and M. P. González-Marcos, *Catalysts*, 2021, **11**, 1450.
63 G. Penche, M. P. González-Marcos and J. R. González-Velasco, *Top. Catal.*, 2022, **65**, 1541–1555.
64 T. L. Nash, G. W. Beall, B. Lee and C. Higgins, *Sci. Adv. Mater.*, 2014, **6**, 703–713.
65 S. J. Yu, Y. Liu, S. J. Byeon, D. W. Park and I. Kim, *Catal. Today*, 2014, **232**, 75–81.
66 N. Nakamoto, *Infrared and raman spectra of inorganic and coordination compounds: Part A: Theory and applications in inorganic chemistry*, John Wiley & Sons, Hoboken, 6th edn, 2008.
67 A. Cano, I. Monroy, M. Ávila, D. Velasco-Arias, J. Rodríguez-Hernández and E. Reguera, *New J. Chem.*, 2019, **43**, 18384–18393.
68 K. R. Dunbar and R. A. Heintz, in *Progress in inorganic chemistry*, ed. K. D. Karlin, John Wiley & Sons, Hoboken, 1997, ch. 4, vol. 45, pp. 283–391.
69 T. Niu, G. Crisci, J. Lu and A. J. Jacobson, *Acta Crystallogr., Sect. C: Cryst. Struct. Commun.*, 1998, **54**, 565–567.
70 A. L. Goodwin, M. T. Dove, A. M. Chippindale, S. J. Hibble, A. H. Pohl and A. C. Hannon, *Phys. Rev. B: Condens. Matter Mater. Phys.*, 2009, **80**, 054101.
71 A. Chruściel, W. Hreczuch, K. Czaja and B. Sacher-Majewska, *Thermochim. Acta*, 2016, **630**, 78–89.
72 M. Thommes, K. Kaneko, A. V. Neimark, J. P. Olivier, F. Rodriguez-Reinoso, J. Rouquerol and K. S. W. Sing, *Pure Appl. Chem.*, 2015, **87**, 1051–1069.
73 K. A. Cychosz, R. Guillet-Nicolas, J. García-Martínez and M. Thommes, *Chem. Soc. Rev.*, 2017, **46**, 389–414.
74 J. C. Groen, L. A. A. Peffer and J. Pérez-Ramírez, *Microporous Mesoporous Mater.*, 2003, **60**, 1–17.
75 C. Marquez, M. Rivera-Torrente, P. P. Paalanen, B. M. Weckhuysen, F. G. Cirujano, D. De Vos and T. De Baerdemaeker, *J. Catal.*, 2017, **354**, 92–99.
76 P. S. Sreeprasanth, R. Srivastava, D. Srinivas and P. Ratnasamy, *Appl. Catal., A*, 2006, **314**, 148–159.
77 A. R. Jadhav, H. A. Bandal and H. Kim, *J. Chem. Eng.*, 2016, **295**, 376–383.
78 S. J. Hibble, A. M. Chippindale, A. H. Pohl and A. C. Hannon, *Angew. Chem., Int. Ed.*, 2007, **46**, 7116–7118.
79 C. H. Tran, L. T. T. Pham, Y. Lee, H. B. Jang, S. Kim and I. Kim, *J. Catal.*, 2019, **372**, 86–102.
80 X. H. Zhang, Z. J. Hua, S. Chen, F. Liu, X. K. Sun and G. R. Qi, *Appl. Catal., A*, 2007, **325**, 91–98.
81 J. M. Asua, in *Polymer reaction engineering*, ed. J. M. Asua, John Wiley & Sons, Hoboken, 2007, ch. 1, pp. 1–28.
82 B. Nörnberg and G. A. Luinstra, *Eur. Polym. J.*, 2015, **73**, 297–307.